Model-order reduced full-wavefield migration using proper orthogonal decomposition

Hoogerbrugge, L.; Khalid, M. H.; Van Dongen, K. W.A.; Verschuur, D. J.

DOI
10.1093/gji/ggaf356

Publication date
2025

Document Version
Final published version

Published in
Geophysical Journal International

Citation (APA)
Hoogerbrugge, L., Khalid, M. H., Van Dongen, K. W. A., & Verschuur, D. J. (2025). Model-order reduced full-wavefield migration using proper orthogonal decomposition. *Geophysical Journal International*, *243*(2), Article ggaf356. https://doi.org/10.1093/gji/ggaf356

Geophysical Journal International

Geophys. J. Int. (2025) **243,** 1–10
Advance Access publication 2025 September 11
Research Paper
https://doi.org/10.1093/gji/ggaf356

Model-order reduced full-wavefield migration using proper orthogonal decomposition

L. Hoogerbrugge ,[1] M.H. Khalid,[2] K.W.A. van Dongen[1] and D.J. Verschuur[3]

[1] *Department of Imaging Physics, Delft University of Technology, 2628 CD Delft, Netherlands. E-mail: hoogerbrugge.l.a@gmail.com*
[2] *Department of Applied Mathematics, University of Twente, 7522 NB Enschede, Netherlands*
[3] *Department of Applied Geophysics & Petrophysics, Delft University of Technology, 2628 CD Delft, Netherlands*

Accepted 2025 September 1. Received 2025 June 20; in original form 2024 December 22

SUMMARY

As seismic migration is increasingly applied to more and more complex media, more sophisticated imaging techniques are required to generate accurate images of the subsurface. Currently, the best results for imaging are achieved by least-squares migration methods, such as least-squares reverse time migration and full-wavefield migration (FWM). These methods iteratively update the image to minimize the misfit between the forward modelled wavefield and the recorded data at the surface. However, a key challenge for these techniques is the speed of convergence. To accelerate the speed of convergence, pre-conditioning is commonly applied. The most common pre-conditioner is the reciprocal of the Hessian operator. However, this operator is computationally expensive to calculate, making it difficult to apply directly. In this paper, we present a novel, alternative, pre-conditioner for FWM. This pre-conditioner is based on applying Galerkin projections to a linear system, which projects the system onto a set of known basis vectors. To find an appropriate set of basis vectors for this approach we apply proper orthogonal decomposition (POD) to a set of partial solutions of the linear system. The resulting method gives an approximation to the pseudo-inverse based on these basis vectors. To test this technique, which we name model-order reduced FWM (MOR-FWM), we apply it to the synthetic Marmousi model as well as to field data from the Vøring basin in Norway. For these examples, we show that MOR-FWM yields an improved data-misfit compared to the standard FWM approach. In addition, we show that the result for the field data case can be improved by normalizing the partial solutions before applying POD.

Key words: Inverse theory; Numerical modelling; Numerical solutions..

1 INTRODUCTION

Seismic migration is an important tool for subsurface characterization, which is of vital importance in many different areas. Examples include the study of the Earth's geological structures, the location of subsurface resources and the characterization of potential sites for off-shore wind farms (Brune *et al.* 2022), to name a few.

While many different approaches for seismic migration exist (Bee Bednar 2005), the general approach commonly consists of three steps. First, the source wavefield at the surface is propagated forward into the medium through a numerical forward modelling scheme, where an estimate of the, generally unknown, speed-of-sound model is used to ensure accurate propagation. Secondly, using a similar approach, the measured data at the subsurface is propagated backwards in time into the medium. Finally, the forward and backward propagated wavefields are correlated using an imaging condition, leading to an estimate of the reflectivity model of the subsurface.

To improve upon the standard migration approach, Least-Squares Migration (LSM) methods have been introduced (Schuster 1993; Nemeth *et al.* 1999). LSM methods aim to minimize the misfit between the recorded data and forward modelled wavefield at the surface by iteratively updating the reflectivity model of the subsurface. While these methods come with an increase in computational costs due to their iterative nature, the resolution of the final reflectivity image can be drastically improved, as LSM techniques can suppress artifacts due to irregular acquisition geometries, band-limited source functions and geometric spreading, among others (Huang *et al.* 2014).

The current gold standard of LSM is Least-Squares Reverse-Time Migration (LS-RTM; Dai & Schuster 2010). LS-RTM techniques generally use two-way, finite-difference modelling to model the forward- and back-propagated wavefields within the subsurface, after which an imaging condition is applied to update the reflectivity model. Using this approach, accurate images of the subsurface can be recovered, even at large offsets. However, these techniques are generally expensive computationally, and often struggle in areas with strong multiple-scattering events.

An alternative approach is given by full-wavefield migration (FWM) (Berkhout 2014b; Davydenko & Verschuur 2017), which models the wavefield using one-way convolutional operators in the space-frequency domain. Due to its use of one-way propagators, FWM exhibits a reduced computational cost compared to full, two-way modelling (Mulder & Plessix 2004), at the expense of less accurate propagation at large angles and an inability to accurately model diving waves. Additionally, by using iterative Neumann modelling, FWM incorporates multiple scattering effects in the imaging algorithm, making it well-suited in areas with strong mulitple-scattering events.

A key challenge for all LSM techniques is the speed of convergence of the iterative method. In most cases, some form of gradient descent is used to iteratively update the reflectivity model. However, standard gradient descent algorithms typically suffer from slow convergence (Pratt *et al.* 1998). To accelerate their convergence, pre-conditioning can be applied. The most common pre-conditioner used in the context of LSM is the reciprocal of the Hessian operator (Pratt *et al.* 1998). As this operator is computationally expensive to calculate, approximations of the Hessian are commonly applied to reduce the computational complexity (Beydoun & Mendes 1989; Abolhassani & Verschuur 2024). In recent years, alternative approaches for constructing pre-conditioners have also been introduced, based on finding approximations of the pseudo-inverse operator (Hou & Symes 2015; Chauris & Cocher 2017).

In this paper, we extend FWM with a novel pre-conditioner, based on approximating the normal equations using proper orthogonal decomposition (POD; Moore 1981; Sirovich 1987; Berkooz *et al.* 1993; Kunisch & Volkwein 2001). POD is a model-order reduction technique which extracts the dominant modes of partial solutions of a large-scale problem, such as LSM, to create a smaller, easier to solve problem. Model-order reduction techniques have a rich history (Rozza *et al.* 2008; Quarteroni *et al.* 2016), and have been successfully applied to both seismic imaging and inversion problems (Mamonov *et al.* 2015; Borcea *et al.* 2023), as well as problems in seismology (Hawkins *et al.* 2023). Model-order reduction techniques have also been used to generate pre-conditioners for related problems (Borcea *et al.* 2014). However, up to now these methods have not been applied to FWM, which we present in this paper.

To explore this new method, which we name model-order reduced FWM (MOR-FWM), we first give a general description of the FWM method. Next, we discuss the POD method and illustrate how this can be used as a pre-conditioner for FWM. Note that this approach can easily be extended to other least-squares migration techniques, which makes the method of broader interest. The pre-conditioned FWM algorithm is then tested on both the synthetic Marmousi model as well as on a field data set from the Vøring basin. Finally, we end with a discussion of these results as well as our final conclusions.

2 THEORY

This section is split into two parts. In the first section, we give a concise overview of the full-wavefield modelling (FWMod) and FWM methods. Interested readers are encouraged to examine earlier work for a more comprehensive description of these methods (Berkhout 2014a, b; Staal 2015; Davydenko & Verschuur 2017). In the second section, we describe the MOR-FWM method, which uses Galerkin projections and POD to create a pre-conditioner.

Algorithm 1: Full Wavefield Modelling (FWMod)

```
Result: $\mathbf{p}_K^+(z_n)$ and $\mathbf{p}_K^-(z_n)$ for all $z_n$
Input: $\boldsymbol{\sigma}(z_0)$
Set $\mathbf{p}_0^-(z_n) = \mathbf{0}$ for all $z_n$;
for $k = 1 : K$ do
    Set $\mathbf{p}_k^+(z_0) = \boldsymbol{\sigma}(z_0)$;
    for $n = 0 : N_z - 1$ do
        $\mathbf{q}_k^+(z_n) = \mathbf{R}^\cap(z_n)\mathbf{p}_{k-1}^-(z_n) + \mathbf{T}^+(z_n)\mathbf{p}_k^+(z_n)$;
        $\mathbf{p}_k^+(z_{n+1}) = \mathbf{W}(z_{n+1}, z_n)\mathbf{q}_k^+(z_n)$;
    end
    Set $\mathbf{p}_k^-\left(z_{N_z}\right) = \mathbf{0}$;
    for $n = N_z : -1 : 2$ do
        $\mathbf{q}_k^-(z_n) = \mathbf{R}^\cup(z_n)\mathbf{p}_k^+(z_n) + \mathbf{T}^-(z_n)\mathbf{p}_k^-(z_n)$;
        $\mathbf{p}_k^-(z_{n-1}) = \mathbf{W}(z_{n-1}, z_n)\mathbf{q}_k^-(z_n)$;
    end
end
```

2.1 Full-wavefield modelling and migration

We begin by examining a 2-D version of the forward modelling algorithm FWMod. FWMod is based on splitting the full, acoustic, wavefield into up- and down-going wavefields. Following Berkhout (2014a) and Davydenko & Verschuur (2017), we give the relationship between the up- and down-going wavefields at an interface located at $z = z_n$ for angular frequency ω, hence

$$\mathbf{q}^+(z_n) = \mathbf{R}^\cap(z_n)\,\mathbf{p}^-(z_n) + \mathbf{T}^+(z_n)\,\mathbf{p}^+(z_n)\,, \tag{1}$$

$$\mathbf{q}^-(z_n) = \mathbf{R}^\cup(z_n)\,\mathbf{p}^+(z_n) + \mathbf{T}^-(z_n)\,\mathbf{p}^-(z_n)\,, \tag{2}$$

where $\mathbf{q}^+(z_n)$, $\mathbf{q}^-(z_n)$, $\mathbf{p}^+(z_n)$ and $\mathbf{p}^-(z_n)$ are complex vectors of length N_x, with N_x the number of gridpoints in the lateral (x) direction, with $(\mathbf{q}/\mathbf{p})^\pm(z_n)\big|_i = (q/p)^\pm(x_i, z_n)$. The symbols q and p denote waves travelling away from and towards the interface, respectively, while the superscripts $^+$ and $^-$ denote down- and up-going wavefields, respectively. The matrices $\mathbf{R}^\cup(z_n)$, $\mathbf{R}^\cap(z_n)$, $\mathbf{T}^+(z_n)$ and $\mathbf{T}^-(z_n)$ are real and of size $N_x \times N_x$, where $\mathbf{R}^\cup(z_n)$ and $\mathbf{R}^\cap(z_n)$ are the reflectivity operators for waves striking the interface from above and below, respectively, while $\mathbf{T}^+(z_n)$ and $\mathbf{T}^-(z_n)$ are the transmission operators for waves striking the interface from above and below, respectively. In a similar way, we give the relationship between wavefields at different depth levels, viz.

$$\mathbf{p}^+(z_{n+1}) = \mathbf{W}(z_{n+1}, z_n)\,\mathbf{q}^+(z_n)\,, \tag{3}$$

$$\mathbf{p}^-(z_{n-1}) = \mathbf{W}(z_{n-1}, z_n)\,\mathbf{q}^-(z_n)\,, \tag{4}$$

where the propagation operators $\mathbf{W}(z_{n+1}, z_n)$ and $\mathbf{W}(z_{n-1}, z_n)$ are complex matrices of size $N_x \times N_x$ describing the propagation between neighbouring depth levels. By recursively applying eqs (1)–(4) we can model the wavefield at every depth level. This process is described in algorithm 1. Note the introduction of the vector $\boldsymbol{\sigma}(z_0)$ and scalar K in algorithm 1, where $\boldsymbol{\sigma}(z_0)$ is a complex vector of length N_x which describes the source wavefield at the surface z_0, while K denotes the number of round-trips modelled. For each round-trip, the order of (internal) multiples modelled increases by one.

The procedure described in algorithm 1 can also be represented by the following forward modelling equations

$$\mathbf{p}_k^+(z_n) = \overline{\mathbf{W}}^+(z_n, z_0)\,\boldsymbol{\sigma}(z_0) + \sum_{m=0}^{n-1} \overline{\mathbf{W}}^+(z_n, z_m)\,\mathbf{R}^\cap(z_m)\,\mathbf{p}_{k-1}^-(z_m), \tag{5}$$

$$\mathbf{p}_k^-(z_n) = \sum_{m=n+1}^{N_z} \overline{\mathbf{W}}^-(z_n, z_m)\,\mathbf{R}^{\cup}(z_m)\,\mathbf{p}_k^+(z_m), \tag{6}$$

where, following Staal (2015), we have introduced the generalized propagation operators

$$\overline{\mathbf{W}}^+(z_n, z_m) = \left[\prod_{i=n-1}^{m+1} \mathbf{W}(z_{i+1}, z_i)\,\mathbf{T}^+(z_i)\right]\mathbf{W}(z_{m+1}, z_m), \tag{7}$$

$$\overline{\mathbf{W}}^-(z_n, z_m) = \left[\prod_{i=n+1}^{m-1} \mathbf{W}(z_{i-1}, z_i)\,\mathbf{T}^-(z_i)\right]\mathbf{W}(z_{m-1}, z_m). \tag{8}$$

We start examining the FWM inversion method using eqs (5)–(8). Consider a small perturbation $\hat{\mathbf{R}}(z_n)$ to the background reflectivity operator $\mathbf{R}_0^{\cup}(z_n)$, viz. $\mathbf{R}^{\cup}(z_n) = \mathbf{R}_0^{\cup}(z_n) + \hat{\mathbf{R}}(z_n)$. Using continuity of the wavefields at an interface, we find $\mathbf{R}^{\cap} = -\mathbf{R}^{\cup}$, $\mathbf{T}^+ = \mathbf{I} + \mathbf{R}^{\cup}$ and $\mathbf{T}^- = \mathbf{I} + \mathbf{R}^{\cap}$, which gives

$$\mathbf{R}^{\cup/\cap}(z_n) = \mathbf{R}_0^{\cup/\cap}(z_n) \pm \hat{\mathbf{R}}(z_n), \tag{9}$$

$$\mathbf{T}^{\pm}(z_n) = \mathbf{T}_0^{\pm}(z_n) \pm \hat{\mathbf{R}}(z_n). \tag{10}$$

We now substitute eqs (9) and (10) into eqs (5) and (6) and model the background wavefields $\mathbf{p}_{0,k}^{\pm}$ propagating in the unperturbed, heterogeneous medium described by $\mathbf{R}_0^{\cup/\cap}(z_n)$ and $\mathbf{W}(z_{n\pm1}, z_n)$, hence

$$\mathbf{p}_{0,k}^+(z_n) = \overline{\mathbf{W}}_0^+(z_n, z_0)\,\boldsymbol{\sigma}(z_0) + \sum_{m=0}^{n-1} \overline{\mathbf{W}}_0^+(z_n, z_m)\,\mathbf{R}_0^{\cap}(z_m)\,\mathbf{p}_{0,k-1}^-(z_m), \tag{11}$$

$$\mathbf{p}_{0,k}^-(z_n) = \sum_{m=n+1}^{N_z} \overline{\mathbf{W}}_0^-(z_n, z_m)\,\mathbf{R}_0^{\cup}(z_m)\,\mathbf{p}_{0,k}^+(z_m). \tag{12}$$

Next, we model the additional wavefields $\hat{\mathbf{p}}_k^{\pm}$ arising from the perturbations $\hat{\mathbf{R}}(z_n)$. Ignoring second-order scattering due to these perturbations, we find

$$\hat{\mathbf{p}}_k^+(z_n) = \sum_{m=1}^{n-1} \overline{\mathbf{W}}_0^+(z_n, z_m)\,\hat{\mathbf{R}}(z_m)\left(\mathbf{p}_{0,k}^+(z_m) - \mathbf{p}_{0,k-1}^-(z_m)\right), \tag{13}$$

$$\hat{\mathbf{p}}_k^-(z_n) = \sum_{m=n+1}^{N_z} \overline{\mathbf{W}}_0^-(z_n, z_m)\left[\mathbf{R}_0^{\cup}(z_m)\,\hat{\mathbf{p}}_i^+(z_m) + \hat{\mathbf{R}}(z_m)\left(\mathbf{p}_{0,k}^+(z_m) - \mathbf{p}_{0,k}^-(z_m)\right)\right]. \tag{14}$$

Note the use of the subscript $_0$ to denote wavefields and operators in the unperturbed background medium, and the use of the caret symbol ˆ to denote wavefields and operators due to the perturbation $\hat{\mathbf{R}}(z_n)$.

We now assume the reflectivity operator to be angle-independent, which is a reasonable approximation at small angles. With this assumption, $\mathbf{R}_0^{\cup}(z_n)$ and $\hat{\mathbf{R}}(z_n)$ are diagonal matrices. Assuming $\mathbf{p}_{0,k-1}^-(z_n) \approx \mathbf{p}_{0,k}^-(z_n)$, the upgoing wavefield at the surface is then given by

$$\hat{\mathbf{p}}_k^-(z_0) = \sum_{m=0}^{N_z} \left(\overline{\mathbf{W}}_0^{\cup}(z_0, z_m) + \overline{\mathbf{W}}_0^-(z_0, z_m)\right)\hat{\mathbf{r}}(z_m) \circ \left(\mathbf{p}_{0,k}^+(z_m) - \mathbf{p}_{0,k}^-(z_m)\right), \tag{15}$$

where $\circ$ represents the Hadamard product, and we have introduced $\hat{\mathbf{r}}(z_m)$, a real vector of length N_x with elements $\hat{\mathbf{r}}(z_m)\big|_i = \hat{\mathbf{R}}(z_m)\big|_{ii}$, and

$$\overline{\mathbf{W}}_0^{\cup}(z_0, z_n) = \sum_{m=n+1}^{N_z} \overline{\mathbf{W}}_0^-(z_0, z_m)\,\mathbf{R}_0^{\cup}(z_m)\,\overline{\mathbf{W}}_0^+(z_m, z_n). \tag{16}$$

As the Hadamard product is commutative, we can write

$$\hat{\mathbf{p}}_k^-(z_0) = \sum_{m=0}^{N_z} \left(\overline{\mathbf{W}}_0^{\cup}(z_0, z_m) + \overline{\mathbf{W}}_0^-(z_0, z_m)\right)\left(\mathbf{P}_{0,k}^+(z_m) - \mathbf{P}_{0,k}^-(z_m)\right)\hat{\mathbf{r}}(z_m), \tag{17}$$

where $\mathbf{P}_{0,k}^{\pm}(z_m) = \mathrm{diag}\left(\mathbf{p}_{0,k}^{\pm}(z_m)\right)$. As eq. (17) is linear with respect to $\hat{\mathbf{r}}(z_m)$, it can be written as

$$\hat{\mathbf{p}}_k^-(z_0) = \mathbf{A}_{\omega,\sigma}\,\hat{\mathbf{r}}, \tag{18}$$

where $\mathbf{A}_{\omega,\sigma}$ is a complex matrix of size $N_x \times N_x N_z$, constructed by horizontally tiling the matrices $\left(\overline{\mathbf{W}}_0^{\cup} + \overline{\mathbf{W}}_0^-\right)\left(\mathbf{P}_{0,k}^+ - \mathbf{P}_{0,k}^-\right)$, and $\hat{\mathbf{r}}$ is a real vector of length $N_x N_z$, constructed by vertically tiling the vectors $\hat{\mathbf{r}}(z_m)$. Up until now, we have examined the wavefield at a single frequency ω due to a single source, with corresponding source wavefield $\boldsymbol{\sigma}(z_0)$, as represented by $\mathbf{A}_{\omega,\sigma}$ in eq. (18). The full wavefield for all sources and frequencies can be written as

$$\mathbf{p}_k^{-,\mathrm{full}}(z_0) - \mathbf{p}_{0,k}^{-,\mathrm{full}}(z_0) = \mathbf{A}\hat{\mathbf{r}} \Leftrightarrow \begin{bmatrix} \hat{\mathbf{p}}_k^-(\omega_1, \boldsymbol{\sigma}_1, z_0) \\ \vdots \\ \hat{\mathbf{p}}_k^-(\omega_{N_\omega}, \boldsymbol{\sigma}_{N_\sigma}, z_0) \end{bmatrix} = \begin{bmatrix} \mathbf{A}_{\omega_1,\sigma_1} \\ \vdots \\ \mathbf{A}_{\omega_{N_\omega},\sigma_{N_\sigma}} \end{bmatrix}\hat{\mathbf{r}}, \tag{19}$$

which is constructed by vertically tiling the vectors $\hat{\mathbf{p}}_k^-(z_0)$ and matrices $\mathbf{A}_{\omega,\sigma}$ of eq. (18).

To perform FWM, we first set $\mathbf{p}_k^{-,\mathrm{full}}(z_0) = \mathbf{d}$, with $\mathbf{d}$ a complex vector of length $N_x N_\sigma N_\omega$ containing the recorded wavefield at the surface for all N_σ sources and all N_ω frequencies. We now wish to solve eq. (19) for the reflectivity vector $\hat{\mathbf{r}}$. The most straightforward approach to obtain $\hat{\mathbf{r}}$ is by solving the normal equations, hence

$$\hat{\mathbf{r}} = \left(\mathbf{A}^{\mathbf{H}}\mathbf{A}\right)^{-1}\mathbf{A}^{\mathbf{H}}\left(\mathbf{d} - \mathbf{p}_{0,k}^{-,\mathrm{full}}(z_0)\right), \tag{20}$$

where the superscript $^{\mathbf{H}}$ represents the conjugate transpose. However, this is impractical, as $\mathbf{A}$ is of size $N_x N_\sigma N_\omega \times N_x N_z$ in 2-D. This makes it prohibitively expensive computationally to calculate the matrix inverse. Instead, we define a cost function J, with

$$J = \frac{1}{2}\sum_{i,j}\left\|\left(\mathbf{d}(\omega_i, \boldsymbol{\sigma}_j) - \mathbf{p}_{0,k}^-(\omega_i, \boldsymbol{\sigma}_j, z_0)\right) - \mathbf{A}_{\omega_i,\sigma_j}\hat{\mathbf{r}}\right\|^2, \tag{21}$$

where $\|\ldots\|$ is the Euclidean norm of the vector. We now perform gradient descent to find $\hat{\mathbf{r}}$. As eq. (19) is linear in $\hat{\mathbf{r}}$, the gradient of the cost function J is given by

$$\frac{\partial J}{\partial \hat{\mathbf{r}}} = -\sum_{i,j}\mathrm{Re}\left(\mathbf{A}_{\omega_i,\sigma_j}^{\mathbf{H}}\mathbf{e}_k(\omega_i, \boldsymbol{\sigma}_j)\right), \tag{22}$$

where

$$\mathbf{e}_k(\omega_i, \boldsymbol{\sigma}_j) = \mathbf{d}(\omega_i, \boldsymbol{\sigma}_j) - \mathbf{p}_{0,k}^-(\omega_i, \boldsymbol{\sigma}_j, z_0) - \mathbf{A}_{\omega_i,\sigma_j}\hat{\mathbf{r}}. \tag{23}$$

We now use this gradient to update the reflectivity

$$\mathbf{r}^{\cup} = \mathbf{r}_0^{\cup} + \alpha\frac{\partial J}{\partial \hat{\mathbf{r}}}, \tag{24}$$

where the (real-valued) scalar α is given by

$$\alpha = \frac{\mathrm{Re}\left[\left(\mathbf{A}\frac{\partial J}{\partial \hat{\mathbf{r}}}\right)^{\mathbf{H}}\mathbf{e}_k\right]}{\left\|\mathbf{A}\frac{\partial J}{\partial \hat{\mathbf{r}}}\right\|^2}. \tag{25}$$

Setting $\mathbf{r}_0^{\cup} = \mathbf{r}^{\cup}$, we can now repeat this process for multiple iterations to gradually minimize the cost function J. The full FWM process is summarized in algorithm 2. Note that eqs (22) and (25) can be calculated using a depth-recursive approach similar to the one shown in algorithm 1. This significantly reduces the computational cost of algorithm 2.

Algorithm 2: Conventional Full Wavefield Migration (FWM)

```
Result: Reflectivity model $\mathbf{r}^{\cup}$.
Input: Measured data $\mathbf{d}$
Set $\mathbf{r}^{\cup} = \mathbf{0}$;
for $k = 1 : K$ do
    Set $\mathbf{r}_0^{\cup} = \mathbf{r}^{\cup}$;
    Calculate $\mathbf{p}_{0,k}^{+}(z_n)$ and $\mathbf{p}_{0,k}^{-}(z_n)$ for all $z_n$ using algorithm 1;
    Calculate $\frac{\partial J}{\partial \hat{\mathbf{r}}} = -\sum_{i,j} \mathrm{Re}\left(\mathbf{A}^{\mathbf{H}}_{\omega_i,\sigma_j} \mathbf{e}_k(\omega_i, \boldsymbol{\sigma}_j)\right)$;
    Calculate $\alpha = \mathrm{Re}\left[\left(\mathbf{A}\frac{\partial J}{\partial \hat{\mathbf{r}}}\right)^{\mathbf{H}} \mathbf{e}_k\right] \Big/ \left\|\mathbf{A}\frac{\partial J}{\partial \hat{\mathbf{r}}}\right\|^2$;
    Update reflectivity $\mathbf{r}^{\cup} = \mathbf{r}_0^{\cup} + \alpha \frac{\partial J}{\partial \hat{\mathbf{r}}}$
end
```

2.2 Model-order reduced full-wavefield migration using proper orthogonal decomposition

In this section, we examine an alternative approach to solve eq. (19), based on Galerkin projections and POD. We begin by describing the method of Galerkin projections for a linear system. Assume that the final solution $\hat{\mathbf{r}}$ can be written as a linear combination of N_r known basis vectors $\hat{\mathbf{r}}_{r,i}$ where $N_r \ll N_x N_z$, that is,

$$\hat{\mathbf{r}} \approx \sum_i c_i \hat{\mathbf{r}}_{r,i} = \hat{\mathbf{R}}_r \mathbf{c}, \tag{26}$$

where $\hat{\mathbf{R}}_r$ is a real matrix of size $N_x N_z \times N_r$, with columns $\hat{\mathbf{r}}_{r,i}$, and $\mathbf{c}$ is a vector of the coefficients c_i. Eq. (19) can then be rewritten as

$$\mathbf{A}\hat{\mathbf{R}}_r \mathbf{c} = \mathbf{d} - \mathbf{p}_{0,k}^{-,\mathrm{full}}(z_0)\,. \tag{27}$$

Left-multiplying both sides of eq. (27) by $\left(\mathbf{A}\hat{\mathbf{R}}_r\right)^{\mathbf{H}}$ and taking the inverse gives

$$\mathbf{c} = \left(\begin{bmatrix} \mathrm{Re}\left(\mathbf{A}\hat{\mathbf{R}}_r\right) \\ \mathrm{Im}\left(\mathbf{A}\hat{\mathbf{R}}_r\right) \end{bmatrix}^{\mathbf{H}} \begin{bmatrix} \mathrm{Re}\left(\mathbf{A}\hat{\mathbf{R}}_r\right) \\ \mathrm{Im}\left(\mathbf{A}\hat{\mathbf{R}}_r\right) \end{bmatrix}\right)^{-1} \begin{bmatrix} \mathrm{Re}\left(\mathbf{A}\hat{\mathbf{R}}_r\right) \\ \mathrm{Im}\left(\mathbf{A}\hat{\mathbf{R}}_r\right) \end{bmatrix}^{\mathbf{H}} \begin{bmatrix} \mathrm{Re}\left(\mathbf{d} - \mathbf{p}_{0,k}^{-,\mathrm{full}}(z_0)\right) \\ \mathrm{Im}\left(\mathbf{d} - \mathbf{p}_{0,k}^{-,\mathrm{full}}(z_0)\right) \end{bmatrix}, \tag{28}$$

where we have separated the real and imaginary parts to ensure that the coefficient vector $\mathbf{c}$ is real. After using eq. (28) to find the coefficients c_i, the perturbation $\hat{\mathbf{r}}$ can be computed using eq. (26).

Note the similarity of eq. (28) to eq. (20). Both equations represent solving the normal equations of eq. (19). However, eq. (20) requires taking the inverse of a matrix of size $N_x N_z \times N_x N_z$, while eq. (28) reduces the size of this matrix to $N_r \times N_r$. Therefore, in situations where one can find a small set of basis vectors $\hat{\mathbf{r}}_{r,i}$ that describe the full solution $\hat{\mathbf{r}}$ such that $N_r \ll N_x N_z$, the method of Galerkin projections can dramatically reduce the cost of calculating the inverse. This method can be applied generally to any linear system, given that one can find an appropriate set of basis vectors $\hat{\mathbf{r}}_{r,i}$.

Also note the similarity of this approach to conjugate gradient methods, where the basis vectors $\hat{\mathbf{r}}_{r,i}$ are chosen as a set of conjugate directions (Hestenes & Stiefel 1952). To find these conjugate directions, an iterative scheme is applied in general. The downside of this approach is that the wavefield perturbations $\mathbf{A}\hat{\mathbf{r}}_{r,i}$ cannot be calculated in parallel, as the basis vector $\hat{\mathbf{r}}_{r,i}$ depends on the previous wavefield perturbations $\mathbf{A}\hat{\mathbf{r}}_{r,j}$ for $j < i$. By using POD we can construct a set of basis vectors $\hat{\mathbf{r}}_{r,i}$ *a priori*, which allows $\mathbf{A}\hat{\mathbf{r}}_{r,i}$ to be calculated in parallel, reducing the computational cost of the method.

To find an appropriate set of basis vectors $\hat{\mathbf{r}}_{r,i}$ to form $\hat{\mathbf{R}}_r$ we apply POD. Hence, we will construct $\hat{\mathbf{r}}_{r,i}$ from a set of partial solutions $\mathbf{s}_j$ for $j = 1, \ldots, N_s$, such that $N_r \ll N_s \ll N_x N_z$. These partial solutions may be solutions for a part of the domain, solutions to related problems, or low-fidelity solutions acquired by applying a less expensive approach. To construct $\hat{\mathbf{R}}_r$ from these partial solutions $\mathbf{s}_j$, we begin by constructing the so-called solution matrix $\mathbf{S}$, which is a real matrix of size $N_x N_z \times N_s$, with columns $\mathbf{s}_j$. Next, we take the Singular Value Decomposition (SVD) of $\mathbf{S}$ such that $\mathbf{U}\Sigma\mathbf{V}^{\mathbf{T}} = \mathbf{S}$. The basis vectors $\hat{\mathbf{r}}_{r,i}$ are then given by the columns $\mathbf{u}_i$ of the matrix $\mathbf{U}$. The number of basis vectors required depends on the decay of the singular values $\Sigma|_{ii}$. The faster the decay of the singular values, the fewer basis vectors $\hat{\mathbf{r}}_{r,i}$ are required to span the same domain as the domain spanned by the vectors $\mathbf{s}_j$. Note that we assume that the full solution $\hat{\mathbf{r}}$ falls within the span of $\mathbf{s}_j$, as this is required for the resulting vectors $\hat{\mathbf{r}}_{r,i}$ of the POD process to be appropriate basis vectors for $\hat{\mathbf{r}}$.

To apply POD to FWM, we must therefore first construct an appropriate solution matrix $\mathbf{S}$. Recalling the conventional FWM approach described in Section 2.1, we find that a natural choice for the partial solution vectors $\mathbf{s}_j$ is provided by the components of the gradient $\frac{\partial J}{\partial \hat{\mathbf{r}}}$, that is,

$$\mathbf{S} = \left[\,\mathrm{Re}\left(\mathbf{A}^{\mathbf{H}}_{\omega_1,\sigma_1} \mathbf{e}_k(\omega_1, \boldsymbol{\sigma}_1)\right) \ \ldots \ \mathrm{Re}\left(\mathbf{A}^{\mathbf{H}}_{\omega_{N_\omega},\sigma_{N_\sigma}} \mathbf{e}_k(\omega_{N_\omega}, \boldsymbol{\sigma}_{N_\sigma})\right)\right]. \tag{29}$$

With this choice, the partial solution vectors $\mathbf{s}_j$ represent the contribution to the gradient for a single frequency ω and a single source σ, which can be calculated efficiently for each iteration using algorithm 2. The linear combination $\hat{\mathbf{R}}_r \mathbf{c}$ can therefore be seen as a weighted version of the steepest descent gradient $\frac{\partial J}{\partial \hat{\mathbf{r}}}$, allowing certain frequencies or sources to be given more weight in the construction of the update direction.

Next, we calculate the SVD of the solution matrix $\mathbf{S}$ and construct the low-rank solution matrix $\hat{\mathbf{R}}_r$ from the left singular vectors $\mathbf{u}_i$ as follows:

$$\hat{\mathbf{R}}_r = \left[\,\frac{\partial J}{\partial \hat{\mathbf{r}}}\ \tilde{\mathbf{u}}_1 \ldots \tilde{\mathbf{u}}_{N_\Sigma}\,\right], \tag{30}$$

with N_Σ the maximum rank we choose to take into account, which can be chosen manually or by using an error criterion. In eq. (30) we have explicitly included the conventional gradient $\frac{\partial J}{\partial \hat{\mathbf{r}}}$ and we have applied a Gram–Schmidt procedure to the vectors $\mathbf{u}_i$ to form the vectors $\tilde{\mathbf{u}}$, which are orthogonal to the conventional gradient. This guarantees that the original gradient always falls in the span of $\hat{\mathbf{r}}_{r,i}$, as this may not be guaranteed if only a small number of singular vectors $\mathbf{u}_i$ are used. In this way, we can guarantee that the reflectivity update produced by MOR-FWM for the linearized problem can never be worse than the update produced by the conventional method.

Using $\hat{\mathbf{R}}_r$, we now apply eq. (28) to calculate the coefficient vector $\mathbf{c}$. Finally, knowing $\hat{\mathbf{R}}_r$ and $\mathbf{c}$, we use eq. (26) to retrieve the reflectivity update, viz. $\hat{\mathbf{r}} = \hat{\mathbf{R}}_r \mathbf{c}$. This process is summarized in algorithm 3.

Algorithm 3: Model-Order Reduced Full Wavefield Migration (MOR-FWM)

```
Result: Reflectivity model $\mathbf{r}^{\cup}$.
Input: Measured data $\mathbf{d}$
Set $\mathbf{r}^{\cup} = \mathbf{0}$;
for $k = 1 : K$ do
    Set $\mathbf{r}^{\cup}_0 = \mathbf{r}^{\cup}$;
    Calculate $\mathbf{p}^{+}_{0,k}(z_n)$ and $\mathbf{p}^{-}_{0,k}(z_n)$ for all $z_n$ using algorithm 1;
    Calculate solution matrix $\mathbf{S}$ using eq.~(??);
    Calculate SVD of $\mathbf{S} \Rightarrow \mathbf{U}\Sigma\mathbf{V}^T = \mathbf{S}$;
    Construct low-rank partial solutions $\hat{\mathbf{r}}_{r,i} = \tilde{\mathbf{u}}_i$;
    Calculate wavefield perturbations $\mathbf{A}\hat{\mathbf{R}}_r$ using a modified
      version of algorithm 1;
    Solve reduced system $\mathbf{A}\hat{\mathbf{R}}_r\mathbf{c} = \mathbf{d} - \mathbf{p}^{-,\mathrm{full}}_{0,k}(z_0)$ using
      eq.~(??);
    Update reflectivity $\mathbf{r}^{\cup} = \mathbf{r}^{\cup}_0 + \hat{\mathbf{R}}_r\mathbf{c}$
end
```

3 NUMERICAL RESULTS

In this section, we examine the results obtained with the MOR-FWM method for a synthetic and a field data example. We compare these results with the reconstructions obtained using the conventional FWM method to illustrate the advantages and disadvantages of the approach introduced in this paper.

3.1 Synthetic example: Marmousi model

We begin with the synthetic example, where we have applied the method on a part of the Marmousi model as an initial test. Note that we have not used the full Marmousi model in order to reduce the overall computational cost of the example. Also, due to the use of one-way operators and angle-independent reflection operators, adding larger offsets will generally not lead to improved results in this example.

Data was generated using a time-domain finite-difference scheme (Thorbecke & Draganov 2011) using a source wavefield with a Ricker wavelet signature. For the imaging, a smoothed version of the true velocity model was used as the background velocity model. The parameters used in the modelling and inversion scheme are given in Table 1. The imaging results are shown in Fig. 1.

Examining Fig. 1, we see that both the conventional FWM method as well as the MOR-FWM method outlined in Section 2.2 have produced a reasonable reconstruction of the reflectivity image corresponding to the underlying velocity and density models. However, while the differences between the results of the two methods are modest, in certain areas the MOR-FWM result shows improved consistency and better resolution compared to the conventional method.

Comparing Figs 1(g) and (h), for example, we see that the MOR-FWM method has done a better job of reconstructing the two layers right above the strong reflector in the middle of the figure (bottom three arrows). We also see that the layers in Fig. 1(h) are a bit sharper (top two arrows). Figs 1(j) and (k) show a similar behaviour. The two layers at the top of the image are better resolved in Fig. 1(k) compared to Fig. 1(j) (top three arrows), and the layers are slightly sharper throughout the MOR-FWM figure (bottom two arrows).

This conclusion is further supported by Fig. 1(c), where we have plotted the cost function J as a function of the iteration number k. From this figure, we see that the MOR-FWM method yields a reduced data residual compared to the conventional FWM method, lending further support for the MOR-FWM method.

3.2 Field data example: Vøring basin

Next, we examine the field data example, where we have tested the method on a marine field data set from the Vøring basin in Norway, using a velocity model generated by Joint-Migration Inversion (see Berkhout 2014c; Staal 2015, for more details). The parameters used for this data set are shown in Table 2 and the results in Fig. 2.

Comparing Figs 2(a) and (b), as well as examining 2(d), we see that the difference between the two methods is significantly smaller than in Section 3. This can also be seen from the cost functional J, shown in Fig. 4(d), we see similar behaviour. Both the conventional FWM method as well as the MOR-FWM method yield very similar values after five iterations. However, we note that the MOR-FWM method outperforms the conventional FWM method when fewer iterations are used. This effect is discussed in more detail in Section 4.2.

4 DISCUSSION

Based on the results shown in Figs 1 and 2, we observe that the MOR-FWM method generates slightly better reconstructions compared to the conventional FWM method. More distinct layers are recovered and the layers are sharper to the eye when the MOR-FWM method is used. This is consistent with the interpretation of the method as a pre-conditioner to the conventional approach. In this section, we compare the computational cost of both methods as well as exploring methods to improve the results further.

4.1 Computational costs

We begin by comparing the computational costs of algorithm 2, which describes the conventional FWM method, and algorithm 3, which describes the MOR-FWM method.

Both algorithms begin by calculating the forward modelled wavefields $\mathbf{p}^{+}_{0,k}(z_n)$ and $\mathbf{p}^{-}_{0,k}(z_n)$ in the background medium, followed by calculating $\mathrm{Re}\left(\mathbf{A}^{\mathbf{H}}_{\omega,\sigma}\mathbf{e}_k(\omega,\boldsymbol{\sigma})\right)$ for all frequencies ω and source wavefields $\boldsymbol{\sigma}(z_0)$, which is either used to calculate the gradient of the cost functional J (conventional FWM, eq. 22), or construct the solution matrix $\mathbf{S}$ (MOR-FWM, eq. 29). Next, in the MOR-FWM algorithm, the SVD of the solution matrix $\mathbf{S}$ is calculated to find the basis vectors $\hat{\mathbf{r}}_{r,i} = \tilde{\mathbf{u}}_i$. Assuming that the maximum rank N_Σ taken into account is much smaller than the number of partial solutions $\mathbf{s}_j$, this step has a negligible computational cost.

The real difference between the two methods lies in the next step, the calculation of the wavefield perturbations $\mathbf{A}\frac{\partial J}{\partial \hat{\mathbf{r}}}$ (algorithm 2, step 6) and $\mathbf{A}\hat{\mathbf{R}}_r$ (algorithm 3, step 8). In the MOR-FWM method, the wavefield perturbations for each basis vector $\hat{\mathbf{r}}_{r,i}$ must be calculated, while in the conventional FWM method only the wavefield perturbation due to the gradient $\frac{\partial J}{\partial \hat{\mathbf{r}}}$ is required. Therefore, this step is more expensive computationally by a factor of N_Σ for the MOR-FWM method, where N_Σ is the number of basis vectors taken into account. As the other steps are either identical or have negligible computational costs, this step fully determines the difference in computational cost between the two methods.

To reduce the computational cost of this step, a number of approaches may be used. First, one can reduce the number basis vectors N_Σ used. This will reduce the computational cost, but may lead to smaller improvements to the reconstruction. Alternatively,

Table 1. Parameters Marmousi model.

Lateral grid spacing Δx	10 m	Vertical grid spacing Δz	5 m
Number of lateral gridpoints N_x	431	Number of vertical gridpoints N_z	500
Peak frequency f_{pk}	17 Hz	Minimum frequency f_{min}	2 Hz
Maximum frequency f_{max}	40 Hz	Number of frequencies N_ω	157
Number of sources N_σ	44	Source spacing $\Delta\sigma$	100 m
Size of full system $N_x N_z$	$2 \cdot 10^5$	Number of singular vectors N_Σ	50
Number of iterations K	8		

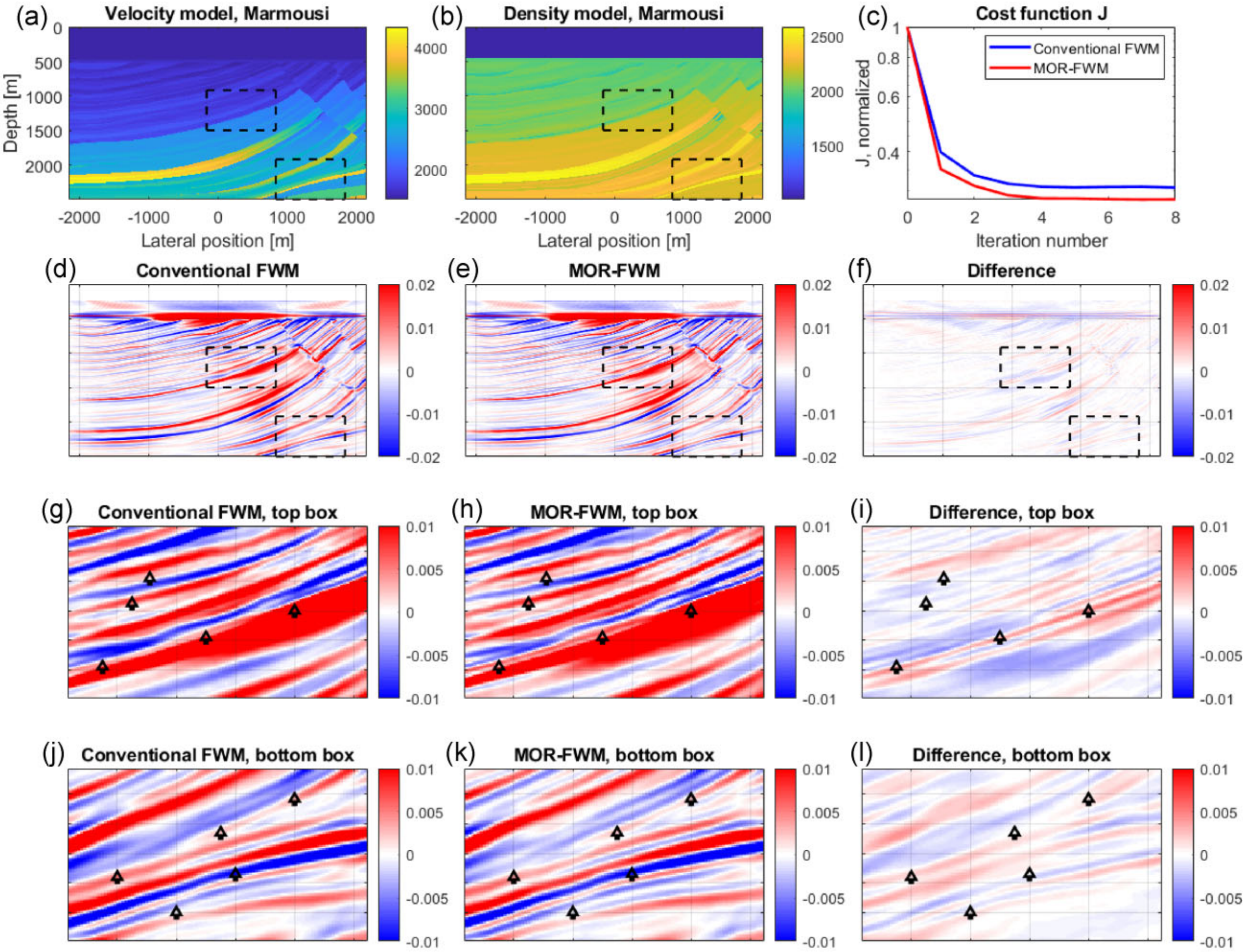

Figure 1. FWM and MOR-FWM results for the synthetic Marmousi example. Panels (a) and (b) show the velocity and density model, respectively, of the part of the Marmousi model under consideration. Panel (c) shows the data residual J, which has been normalized with respect to the residual for $\mathbf{p}^-_{\mathbf{0},\mathbf{1}} = \mathbf{0}$. Panels (d)–(f) show the conventional FWM and MOR-FWM image after eight iterations, respectively, as well as the difference between the two images. Panels (g)–(i) show a zoom-in of the FWM image, the MOR-FWM image and their difference at the location of the top box, respectively, while panels (j)–(l) show zoom-ins of the bottom box. Arrows indicate regions of interest within the figures.

Table 2. Parameters Voring data.

Lateral grid spacing Δx	25 m	Vertical grid spacing Δz	5 m
Number of lateral gridpoints N_x	399	Number of vertical gridpoints N_z	1001
Minimum frequency f_{min}	2 Hz	Maximum frequency f_{max}	60 Hz
Number of frequencies N_ω	293	Number of sources N_σ	23
Source spacing $\Delta\sigma$	450 m	Number of iterations K	5
Size of full system $N_x N_z$	$4 \cdot 10^5$	Number of singular vectors N_Σ	50

other choices for the basis vectors may be explored. For example, alternative choices for the partial solutions $\mathbf{s}_j$ may lead to a more rapid decay of the singular values of the solution matrix $\mathbf{S}$, in which case fewer basis vectors are required to yield a high-quality pre-conditioner. Finally, if the basis vectors $\hat{\mathbf{r}}_{r,i}$ can be estimated a priori, the construction of the solution matrix $\mathbf{S}$ and its SVD can be omitted, and the calculation of $\mathbf{A}\hat{\mathbf{R}}_r$ can be performed offline, as it does not depend on the measured data $\mathbf{d}$. Such a situation may arise in monitoring applications, for example, where high-quality estimates of the reflectivity may already exist.

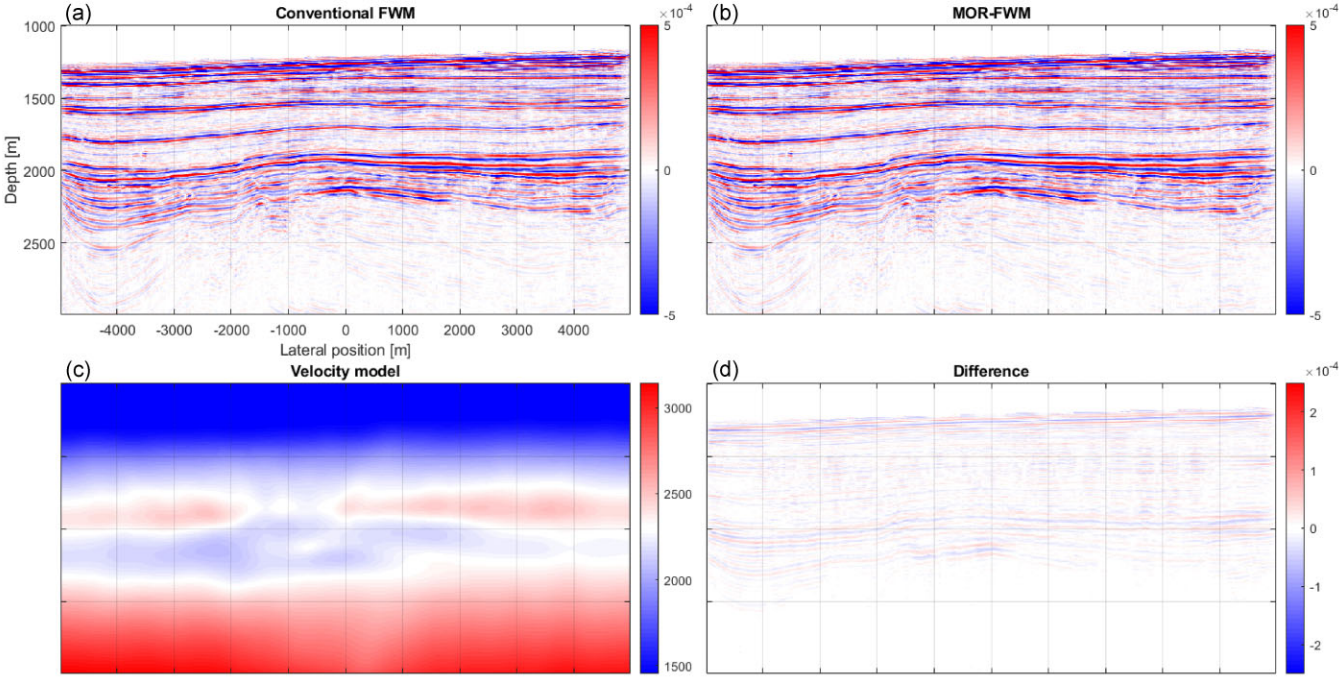

Figure 2. FWM and MOR-FWM results for the Vøring field data example. Panel (c) shows the velocity model used for migration. Panels (a), (b) and (d) show the conventional FWM and MOR-FWM image after five iterations, respectively, as well as the difference between the two images. Note that the difference figures have been plotted with half the clip value of the FWM and MOR-FWM images.

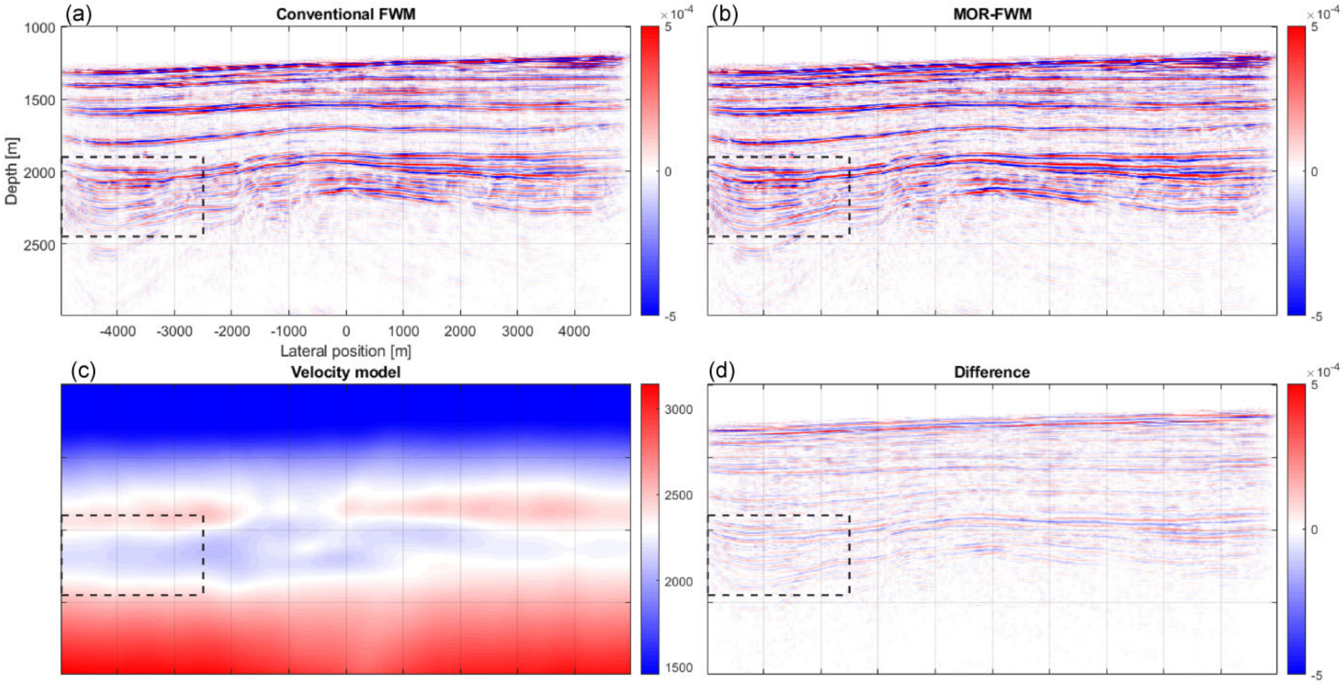

Figure 3. FWM and MOR-FWM results for the Vøring field data example after one iteration. Panels (a), (b) and (d) show the conventional FWM and MOR-FWM image after one iteration, respectively, as well as the difference between the two images. Panel (c) shows the velocity model used for migration. Note that the box plotted in the figures indicates the region displayed in Fig. 4.

4.2 Results after one iteration

Next, we compare the performance of the conventional FWM and the MOR-FWM methods after a single iteration, the results of which are shown in Figs 3 and 4. From this figure, we see that the MOR-FWM method requires fewer iterations to produce a sharp image compared to the conventional method. Comparing Figs 4(a) and (b), for example, we see that the MOR-FWM method displays an improved resolution at the edges of the model at the first iteration (left-most arrow). Also, we see an improved recovery of the strong

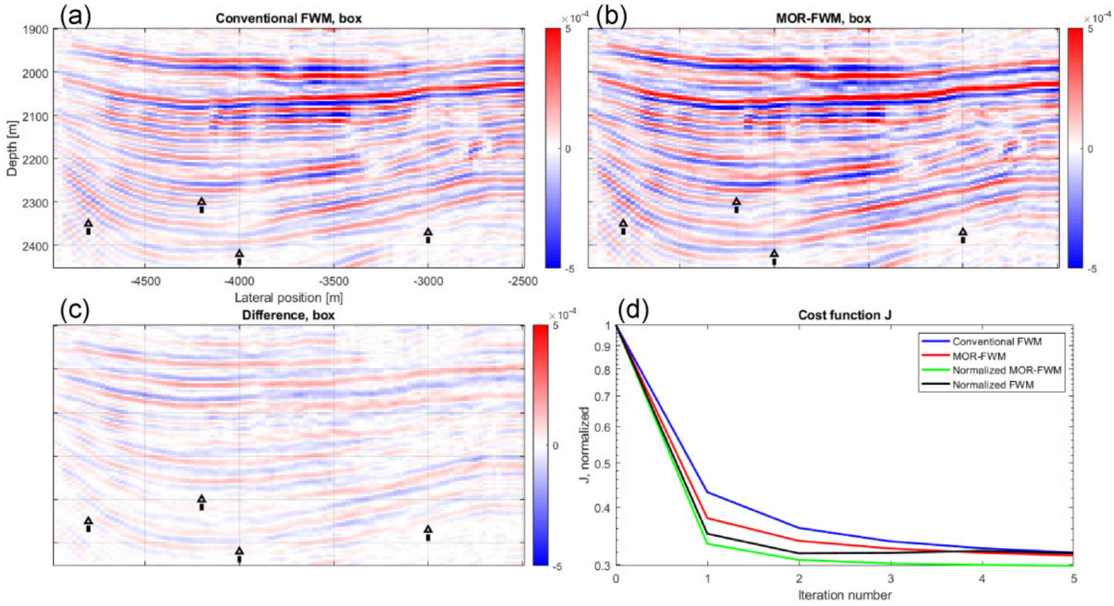

Figure 4. Zoom-in of the FWM and MOR-FWM results for the Vøring field data example after one iteration. Panels (a)–(c) show the conventional FWM and MOR-FWM image after one iteration, respectively, as well as the difference between the two images. Arrows indicate regions of interest within the figures. Panel (a) shows the velocity model used for migration. Panel (d) shows the data residual J, which has been normalized with respect to the residual for $\mathbf{p}^{-}_{0,1} = \mathbf{0}$.

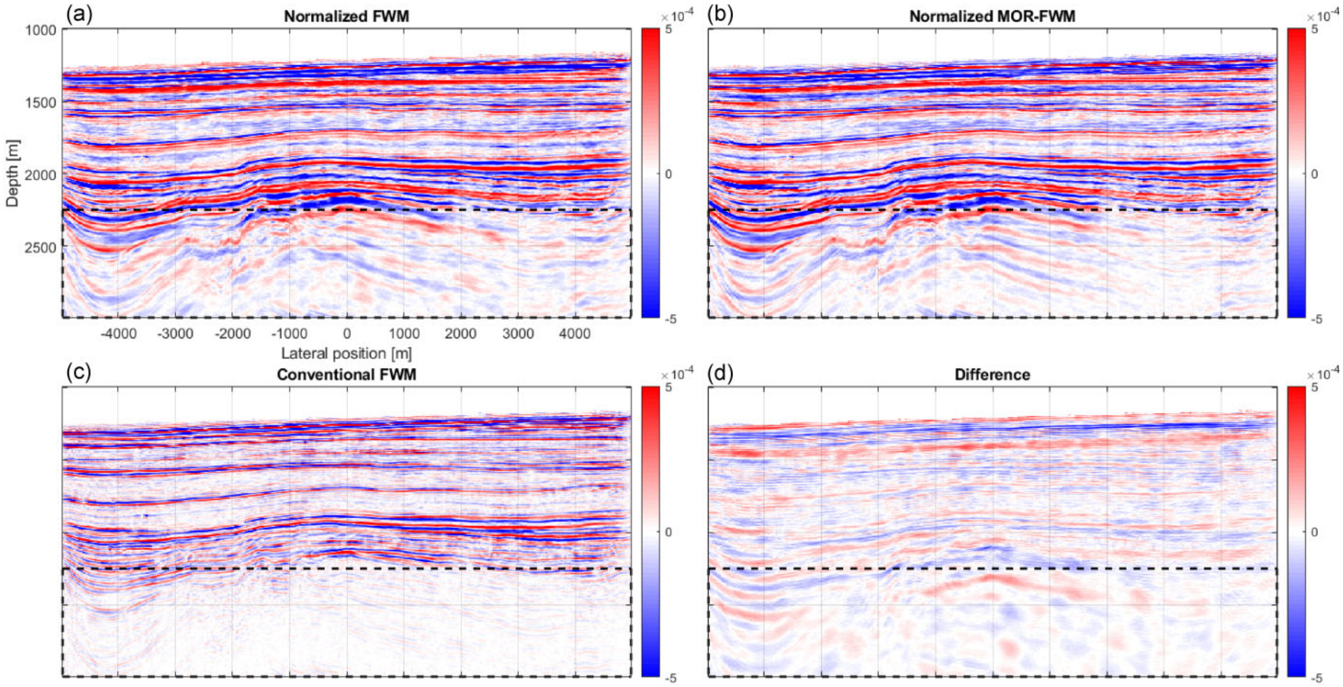

Figure 5. FWM and MOR-FWM results for the Vøring field data example. Panels (a), (b) and d) show the normalized FWM and the normalized MOR-FWM image after five iterations, respectively, as well as the difference between the two images. Panel (c) shows the conventional FWM image for comparison. The box indicates the main region of interest in these figures.

reflectors in the zoomed-in image (top-left arrow). Finally, we see an improved continuity of the weaker reflectors deeper in the image (right and bottom arrows).

This result suggests that, using the MOR-FWM method, one may require fewer iterations to retrieve a sharp image. This is further supported by the cost function J, shown in Fig. 4(d), which shows that the MOR-FWM method achieves a smaller data misfit even at the first iteration. This is especially relevant when FWM is applied in the context of One-way Reflection Waveform Inversion (Abolhassani & Verschuur 2023), also known as Joint Migration Inversion (Berkhout 2014c), where the (background) speed-of-sound model is also updated. In this context it is important to generate an accurate reflectivity model using only a few iterations, as the reflectivity model must be updated each time the speed-of-sound model is adjusted.

4.3 Normalization

Finally, we examine a potential alternative choice for the partial solutions $\mathbf{s}_j$. Recall that the partial solutions $\mathbf{s}_j$ are given by Re $\left(\mathbf{A}^{\mathbf{H}}_{\omega,\sigma}\mathbf{e}_k\left(\omega,\boldsymbol{\sigma}\right)\right)$ for a given frequency ω and source wavefield $\boldsymbol{\sigma}\left(z_0\right)$ (eq. 29). While this is a natural choice, a downside of this approach is that it is sensitive to the source signature. This means that in cases where certain frequencies or sources have larger amplitudes than others, the corresponding partial solutions will also exhibit larger amplitudes. When taking the SVD of the solution matrix $\mathbf{S}$, the basis vectors $\mathbf{u}_i$ will then be weighted towards the partial solutions with the largest amplitudes, meaning that not all sources and frequencies are treated equally in the construction of the basis vectors.

To circumvent this shortcoming, one can choose to normalize each partial solution $\mathbf{s}_j$. This can be done in conventional FWM, where all contributions are simply summed together, or in MOR-FWM, where the normalized partial solutions are used in the SVD. Using this approach, we retrieve the results shown in Fig. 5. Looking at this figure, we see that the imprint of the source signature has been removed, removing a number of spurious reflectors. Due to this effect, we see an improved image in the target zone below the overburden, indicated by the box.

We also note a more pronounced difference between the two methods. Comparing Figs 5(a) and (b), we see that the reflectors in the target zone exhibit a greater continuity when normalized MOR-FWM is applied compared to normalized FWM. This observation is supported by the cost function J, shown in Fig. 4(d), which shows an improved data misfit for normalized MOR-FWM. These results underline the sensitivity of the MOR-FWM method to the choice of basis vectors, as a well-chosen set of basis vectors can significantly improve the results.

5 CONCLUSION

In this paper, we introduce a novel pre-conditioner for full-wavefield migration, using proper orthogonal decomposition to find a reduced basis. We show that this reduced basis can be used to construct a pre-conditioner using Galerkin projections. We tested the resulting algorithm on the synthetic Marmousi model and a field data set from the Vøring basin, where we achieve improved results in both cases compared to the conventional FWM algorithm. We discuss the challenge of the computational cost of the method, which depends linearly on the number of basis vectors used, and present some ideas to further improve the results and/or reduce the computational costs. Based on the flexibility of the method, as well as the results we present in this paper, we conclude that the MOR-FWM method is a useful addition to the existing work on migration in general and FWM in particular.

ACKNOWLEDGMENTS

The authors thank the sponsoring companies from the Delphi Consortium at Delft University of Technology and the research program DeepNL (DeepNL.2018.033), financed by the Dutch Research Council (NWO), for their support of this research. The authors also thank Equinor for providing the Vøring Basin field data, and thank associate professor Matthias Schlottbom for insightful discussions on this work.

DATA AVAILABILITY

The synthetic data used in this paper is available upon request. The field data from the Vøring Basin is freely available from Equinor. Due to agreements made with the sponsoring companies of the Delphi Consortium, we are unable to share the code used to generate the results of this paper.

REFERENCES

Abolhassani, S. & Verschuur, D.J., 2024. Efficient preconditioned least-squares wave-equation migration, *Geophysics,* **89,** doi:10.1190/geo2023-0048.1.

Abolhassani, S. & Verschuur, D.J., 2023. High-resolution one-way reflection waveform inversion, *84th EAGE Annual Conference & Exhibition* **2023,** 1–5

Bee Bednar, J., 2005. A brief history of seismic migration, *Geophysics,* **70,** 3–20.

Berkhout, A.J., 2014a. Review Paper: an outlook on the future of seismic imaging, part I: forward and reverse modelling, *Geophys. Prospect.,* **62,** 911–930.

Berkhout, A.J., 2014b. Review Paper: an outlook on the future of seismic imaging, part II: full-wavefield migration, *Geophys. Prospect.,* **62,** 931–949.

Berkhout, A.J., 2014c. Review Paper: an outlook on the future of seismic imaging, part III: joint migration inversion, *Geophys. Prospect.,* **62,** 950–971.

Berkooz, G., Holmes, P. & Lumley, J.L., 1993. The proper orthogonal decomposition in the analysis of turbulent flows, *Annu. Rev. Fluid Mech.,* **25,** 539–575.

Beydoun, W.B. & Mendes, M., 1989. Elastic ray-Born L2-migration/inversion, *J. Geophys. Int.,* **97,** 151–160.

Borcea, L., Druskin, V., Mamonov, A.V. & Zaslavsky, M., 2014. A model reduction approach to numerical inversion for a parabolic partial differential equation, *Inverse Problems,* **30,** doi:10.1088/0266-5611/30/12/125011.

Borcea, L., Garnier, J., Mamonov, A.V. & Zimmerling, J., 2023. Waveform inversion via reduced order modelling, *Geophysics,* **88,** R175–R191.

Brune, R., Haberkern, J., Wenau, S. & Preu, B., 2022. Ultra-high-resolution marine seismic survey for wind farm site characterization in the German North Sea, *83rd EAGE Annual Conference & Exhibition* **2022** 1–5

Dai, W. & Shushter, G.T., 2010. Multi-source wave equation least-squares migration with a deblurring filter, *72nd EAGE Annual Conference & Exhibition*. **2010** 1–5

Davydenko, M. & Verschuur, D.J., 2017. Full-wavefield migration: using surface and internal multiples in imaging, *Geophys. Prospect.,* **65,** 7–21.

Chauris, H. & Cocher, E., 2017. From migration to inversion velocity analysis, *Geophysics,* **82,** S207–S223.

Hawkins, R., Khalid, M., Smetana, K. & Trampert, J., 2023. Model order reduction for seismic waveform modelling: inspiration from normal modes, *Geophys. J. Int.,* **234,** 2255–2283.

Hestenes, M.R. & Stiefel, E., 1952. Methods of conjugate gradients for solving linear systems, *J. Res. Natl. Bur. Stand.,* **49,** 409–436.

Hou, J. & Symes, W.W., 2015. An approximate inverse to the extended Born modelling operator, *Geophysics,* **80,** R331–R349.

Huang, Y., Dutta, G., Dai, W., Wang, X., Schuster, G.T. & Yu, J., 2014. Making the most out of least-squares migration, *Leading Edge,* **33,** 954–960.

Kunisch, K. & Volkwein, S., 2001. Galerkin proper orthogonal decomposition methods for parabolic problems, *Numer. Math.,* **90,** 117–148.

Mamonov, A.V., Druskin, V. & Zaslavsky, M., 2015. Nonlinear seismic imaging via reduced order model backprojection, *SEG Technical Program Expanded Abstracts*. 4375–4379. doi:10.1190/segam2015-5830429.1.

Moore, B., 1981. Principal component analysis in linear systems: controllability, observability, and model reduction, *IEEE Trans. Automat. Contr.,* **26,** 17–32.

Mulder, W.A. & Plessix, R.-E., 2004. A comparison between one-way and two-way wave-equation migration, *Geophysics,* **69,** 1491–1504.

Nemeth, T., Wu, C. & Shushter, G.T., 1993. Least-squares migration of incomplete reflection data, *Geophysics,* **64,** 13–310.

Pratt, R.G., Shin, C. & Hicks, G.J., 1998. Gauss–Newton and full Newton methods in frequency–space seismic waveform inversion, *J. Geophys. Int.,* **133,** 341–362.

Quarteroni, A., Manzoni, A. & Negri, F., 2016. *Reduced Basis Methods for Partial Differential Equations,* Springer-Verlag, Berlin.

Rozza, G., Huynh, D.B.P. & Patera, A.T., 2008. Reduced basis approximation and a posteriori error estimation for affinely parametrized elliptic coercive partial differential equations: application to transport and continuum mechanics, *Arch. Comput. Methods Eng.,* **15,** 229–275.

Shushter, G.T., 1993. Least-squares cross-well migration, *SEG Technical Program Expanded Abstracts*. 110–113. doi:10.1190/1.1822308.

Sirovich, L., 1987. Turbulence and the dynamics of coherent structures. I. Coherent structures, *Q. Appl. Math.,* **45,** 561–571.

Staal, X.R., 2015. *Combined Imaging and Velocity Estimation by Joint Migration Inversion,* PhD thesis, Delft University of Technology.

Thorbecke, J.W. & Draganov, D., 2011. Finite-difference modelling experiments for seismic interferometry, *Geophysics,* **76,** doi:10.1190/geo2010-0039.1.